

Deep learning surrogate interacting Markov chain Monte Carlo based full wave inversion scheme for properties of materials quantification

Reza Rashednia^{*a}, Mohammad Pour-Ghaz^b

^{a*} *InstroTek Inc., 1 Triangle Dr, Research Triangle Park, Durham, NC 27709, USA,
(Corresponding author) Tel.:+1-979-402-0417. E-mail:reza.rashednia@gmail.com*

^b *Department of Civil Construction and Environmental Engineering, North Carolina State University, Raleigh, NC 27695, USA.*

Abstract

Full Wave Inversion (FWI) imaging scheme has many applications in engineering, geoscience and medical sciences. In this paper, a surrogate deep learning FWI approach is presented to quantify properties of materials using stress waves. Such inverse problems, in general, are ill-posed and nonconvex, especially in cases where the solutions exhibit shocks, heterogeneity, discontinuities, or large gradients. The proposed approach is proven efficient to obtain global minima responses in these cases. This approach is trained based on random sampled set of material properties and sampled trials around local minima, therefore, it requires a forward simulation can handle high heterogeneity, discontinuities and large gradients. High resolution Kurganov-Tadmor (KT) central finite volume method is used as forward wave propagation operator. Using the proposed framework, material properties of 2D media are quantified for several different situations. The results demonstrate the feasibility of the proposed method for estimating mechanical properties of materials with high accuracy using deep learning approaches.

Keywords: Deep Learning, Full Wave Inversion, Inverse problems, Kurganov-Tadmor, Markov chain Monte Carlo, Surrogate Model, Wave propagation.

1. Introduction

Tomography techniques are valuable and widely used in engineering, geoscience and medical sciences. Examples of such tomography based techniques include, Infrared Thermography [1, 2], Electrical Impedance Tomography [3–9], Electrical Capacitance Tomography [10, 11], radar acoustics and Radiography [12, 13], X-Ray Computed Tomography [14–16], and stress wave based tomography [17–33]. Among these methods, stress wave-based methods are attractive since they can provide information about the mechanical properties of materials and structures. Stress wave methods are mostly refraction and reflection

tomography techniques, which use only the travel time kinematics of the transducer data. Full Wave Inversion (FWI) is a type of stress wave tomography which uses complete waveforms and derives high resolution velocity models by minimizing the difference between observed and modeled waveforms. FWI goes beyond refraction and reflection tomography techniques, which use only the travel time kinematics of the signals, by using additional information provided by the amplitude and phase of the stress waveform. The highly detailed models provided by FWI can be used to resolve complex mechanical features both in time and frequency domains[34–38]. There are few research can be applied on deep learning to solve FWI for mechanical behavior reconstruction [39, 40]. This paper provides a computational inverse framework for stress wave FWI tomography to quantify distribution of elastic moduli and densities at the same time or separately.

For numerical inverse solutions of stress wave tomography, nonlinear least-squares, Newtons method or other data-fitting methods can be natural choices commonly used for finding the coefficients in the systems of partial differential equations chosen to model the wave physics. However, they may be cumbersome and computationally expensive to implement for stress wave differential equation specially for finer mesh discretization. Also, gradient-based methods require proper objective functions and constraints for optimal convergence, and they suffer from inability of optimal convergence to global minima in cases of nonconvexity and high ill-posedness and nonlinearity. The numerical implementations of FWI is considered highly non-linear, ill-posed and often nonconvex inverse problem [41]. This becomes worst in the case of materials with large properties gradient, nonlinearity or shock waves. To resolve these issues, we employ a surrogate deep learning interacting Markov chain Monte Carlo based optimization method to solve the FWI inverse problem and estimate properties of materials. In this paper, a surrogate deep-learning optimization approach is presented to minimize the difference between observed and modeled responses. Surrogate deep learning random search naturally causes large properties gradient and high heterogeneity itself. Therefore, this method requires a wave propagation forward modeling which can handle heterogeneity, large properties gradient, nonlinearity and shock waves properly.

Kurganov-Tadmor (KT) high resolution central finite volume scheme is used for solving stress waves in two dimensional heterogeneous media. KT is highly accurate for quantification of materials properties with large properties gradient, nonlinearity or shock waves. This scheme is non-oscillatory and enjoy the main advantage of Godunov-type central schemes: simplicity, i.e., they employ neither characteristic decomposition nor approximate Riemann solvers. This makes it universal method that can be applied to a wide variety of physical problems, including hyperbolic systems of conservation laws. KT central scheme has the numerical dissipation with an amplitude of order $O(\Delta X^3/\Delta t)$ [42]. Beside of the good resolution obtained by the KT, it can use a semi-discrete formulation coupled with an appropriate ODE solver retaining simplicity and high resolution with lower numerical viscosity, proportional to the vanishing size of the time step Δt [42]. This semi-discrete central scheme is based on the ideas of

Rusanovs method using a more precise information about the local speeds of wave propagation computed at each Riemann Problem in two-space dimensions [43]. In this paper, KT is used as forward-wave propagation operator f to map the stress wave velocity to ultrasonic stress wave signals.

In the following, we present KT scheme as the forward model used in this work. Then, deep learning model used in the inverse problem is described. This is followed by deep learning surrogate interacting Markov chain Monte Carlo inverse algorithm. Then, results and discussions are provided and proposed method is investigated on three different examples. Finally, we summarize our findings in conclusions.

2. Forward model: Kurganov-Tadmor scheme

Kurganov-Tadmor (KT) high resolution central scheme recently developed by Kurganov and Tadmor [42], which is one of Monotonic Upwind Schemes for Conservation Laws (MUSCL) [44]. In order to solve partial differential equations, the MUSCL schemes are finite volume schemes that can provide highly accurate numerical solutions for given systems, even in cases where the solutions exhibit shocks, discontinuities, or large gradients. Examples of pioneering works in MUSCL schemes include the first-order Lax Friedrichs scheme [45] and the Nessyahu-Tadmor (NT) scheme [46] which offers higher resolution as compared to the former. Both Lax Friedrichs and NT schemes have a numerical viscosity of the order of $o((\Delta x)^{2r} \setminus \Delta t)$ and suffer from high numerical viscosity when sufficiently small time steps are used ($\Delta t \rightarrow 0$)[42]. KT has a much smaller numerical viscosity of $(o((\Delta x)^{2r-1}))$ which is independent of the $o(1 \setminus \Delta t)$. KT retains the independence of eigen structure of the problem and approximates the solutions of nonlinear conservation laws and convection-diffusion equations with less effort [42]. It also requires much lower number of mesh points containing the wave compared with a first-order methods with similar accuracy. KT provides simple semi-discrete formulation and also uses more precise information of the local propagation speeds which in turn increases the accuracy of the solution. For these reasons, KT is chosen for this study which let us to achieve more accurate FWI results. In this study, KT is developed to solve the stress wave propagation,

$$\frac{\partial^2 u}{\partial t^2} = c^2 \nabla^2 u \quad (1)$$

where $u(x, t)$ is the displacement and c is the constant coefficient.

To use the semi-discrete KT scheme, Equation 1 need to be expressed in first order hyperbolic equation. Therefore, we implement the following change of variables on Equation 1.

$$\frac{\partial}{\partial t} \varepsilon - \frac{\partial}{\partial x} v = 0 \quad (2)$$

$$\frac{\partial}{\partial t} (\rho(x)v) - \frac{\partial}{\partial x} \sigma = 0 \quad (3)$$

where v , ε , σ , and ρ are velocity, strain, stress, and density respectively. In Equation 2, ε is the state variable, and v is the flux. Similarly, in Equation 3, $\rho(x)v$ is the state variable, and σ is the flux.

In KT scheme, linear piecewise approximation of state variable (\hat{u}) is shown by Equation 4 within each cell. Equation 4 is used to discretize Equations 2 and 3 using slope-limited, left and right extrapolated state variable. Hence, high resolution total variation diminishing discretization can be written as Equation 5

$$\hat{u}(x) = \hat{u}_i + \frac{x - x_i}{x_{i+1} - x_i}(\hat{u}_{i+1} - \hat{u}_i) \quad \forall x \in (x_i, x_{i+1}] \quad (4)$$

$$\frac{d\hat{u}_i}{dt} + \frac{1}{\Delta x_i}[f^*(\hat{u}_{i+1/2}) - f^*(\hat{u}_{i-1/2})] = 0 \quad (5)$$

where i is the cell center index. The fluxes $f^*(\hat{u}_{i\pm 1/2})$ are nonlinear combination of the first and second order approximations of the continuous flux function at cell edges. The fluxes, $f^*(\hat{u}_{i\pm 1/2})$, are calculated based on Equations 6 and 7.

$$f^*(\hat{u}_{i-\frac{1}{2}}) = \frac{1}{2}\{[f(\hat{u}_{i-\frac{1}{2}}^R) + f(\hat{u}_{i-\frac{1}{2}}^L)] - a_{i-\frac{1}{2}}[\hat{u}_{i-\frac{1}{2}}^R - \hat{u}_{i-\frac{1}{2}}^L]\} \quad (6)$$

$$f^*(\hat{u}_{i+\frac{1}{2}}) = \frac{1}{2}\{[f(\hat{u}_{i+\frac{1}{2}}^R) + f(\hat{u}_{i+\frac{1}{2}}^L)] - a_{i+\frac{1}{2}}[\hat{u}_{i+\frac{1}{2}}^R - \hat{u}_{i+\frac{1}{2}}^L]\} \quad (7)$$

where R and L are the right and left cells at the $i \pm \frac{1}{2}$ edges. The local propagation speed in each cell edge, $a_{i\pm \frac{1}{2}}$, is the maximum absolute value of the eigenvalue of the Jacobian of $f(\hat{u}(x, t))$, over cell i and $i \pm 1$:

$$a_{i\pm \frac{1}{2}}(t) = \max[\text{abs}(\rho(\frac{\partial f(\hat{u}_i(t))}{\partial \hat{u}})), \text{abs}(\rho(\frac{\partial f(\hat{u}_{i\pm 1}(t))}{\partial \hat{u}}))] \quad (8)$$

where ρ is spectral radius of $\frac{\partial f(\hat{u}(t))}{\partial \hat{u}}$.

We use 2^{nd} Runge Kutta for time integration over $\frac{d\hat{u}_i}{dt}$ after it is found by Equation 5 [42]. Figure 1 presents the flowchart of KT implementation.

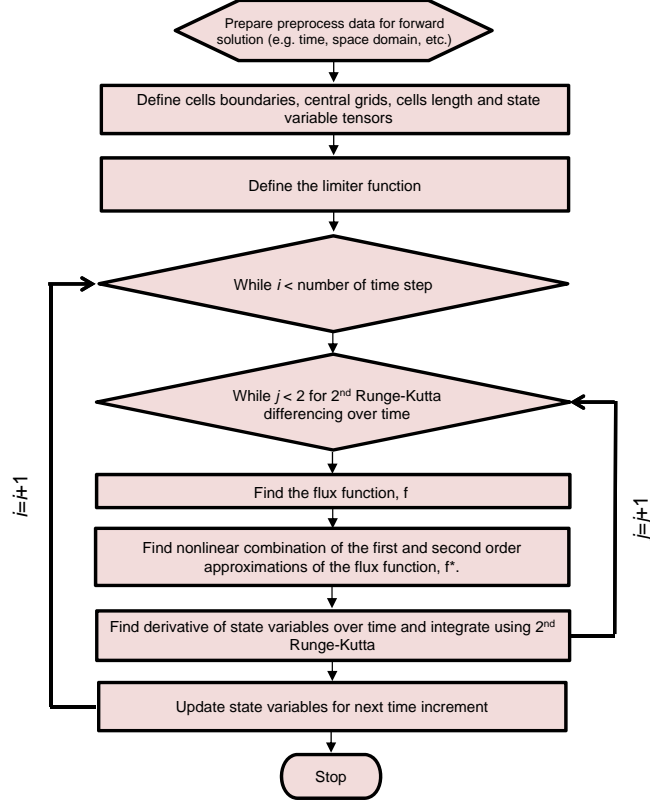


Figure 1: Flowchart of Kurganov-Tadmor central scheme

3. Deep learning model

In this paper, deep neural network with fully connected layers is used to input nodal elastic moduli and densities and output nodal strains over certain boundaries. Figure 2 presents the deep learning architecture in this study. The architecture of this network includes input layer (L_0) of nodal KT material characteristics, hidden layers ($L_1 - L_{H-1}$) and output layer L_H which are nodal strain values over certain boundaries. For these networks, high number of hidden layers are considered to potentially account for the sophisticated nonlinear function mapping the inputs to the outputs, where the number layers and units of these layers will be chosen as hyperparameters based on the networks performance for each example. All hidden layers utilize the tanh activation for modelling the nonlinearity, and the output layer has linear activation to reconstruct strain values. The inverse problem of wave propagation equation is non-convex. In order to deal with non-convexity of the deep network optimization, the Logistic Regression cost function was used. Stochastic Gradient

Descent (SGD) approach was used for network optimization. To improve the model performance, L_2 and dropout regularization approaches were used. L_2 regularization parameters were chosen using an initial batch of random parameter vectors as training and development sets to avoid overfitting (high variance) and underfitting (high bias). To capture better randomness, dropout method was used. Dropout probability is chosen for each example as a regularization hyperparameter. For weight initialization of deep network, Xavier initialization approach is used for faster convergence of optimization. For faster optimization, also mini-batch gradient descent with momentum and RMSprop (Adam method) is used. The mini-batch sizes and momentum terms also will be tuned as hyperparameters. Learning rate and its decay coefficient will be tuned as hyperparameters. In order to tune all deep-learning hyperparameters such as number of hidden layers, layers' units, regularization parameters, mini-batch sizes, Adam hyperparameters and learning rates, initial deep learning network is trained using KT forward models.

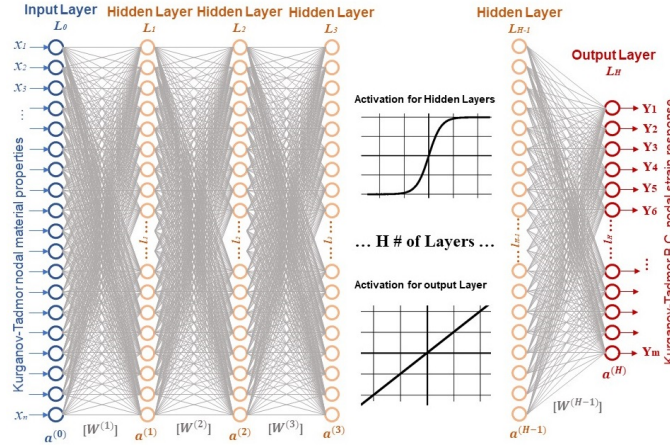


Figure 2: Deep learning architecture.

4. Inverse model: deep learning surrogate interacting Markov chain Monte Carlo search

The inverse problem is addressed as estimation of the mechanical properties of media using stress wave propagation, which has a non-convex error surface with multiple local minima due to data sparsity. Therefore, the gradient-based optimization algorithms may provide convergence to local minima and computationally become highly expensive. Further, high ill-posedness of this inverse problem increases gradient-based algorithms variance which required more complex regularization techniques without guaranteeing better reconstructions.

In this study, Interacting Markov chain Monte Carlo (IMCMC) algorithm is used as the search algorithm in order to find global minima and handle the

data sparsity. Unlike most of the current MCMC methods that ignore the previous trials; here, optimized deep learning model is used to speed-up the Markov Chain Monte Carlo algorithm by an order of magnitude [47]. In this method, the IMCMC method iteratively samples randomly from a sequence of probability distributions and estimating their errors with respect to waveform measurements which increases level of sampling complexity [48]. Then, using the derived data set, a deep learning model is trained based on samplings. Finally, the deep learning model is optimized to estimate the best unknown parameters in order to provide lowest errors with respect to measurements. This sequence is iteratively repeated until the global minima is achieved. The IMCMC method provides sampling from sequence of probability distributions and avoids convergence to local minima.

The objective is to minimize model error function (e^{f^m}), per Equation 9

$$e^{FM}(\vec{p}) = \sum_{i=1}^m \|f_i^{FM}(\vec{p}, \vec{q}) - f_i^{mes}(\vec{q})\|_{L_2(Q)} \quad (9)$$

where $\vec{p} \in \mathbb{R}^n$ are a set of vectors with n unknown material parameters, $\vec{q} \in Q$ is the vector of variables in the measurement domain (e.g., time, boundary conditions), $f_i^{FM}(\vec{p}, \vec{q})$ is the strain response from the forward model (i.e., KT), $f_i^{mes}(\vec{q})$ is the measured strain response, and m is the number of response components. Similarly, the deep learning model error function is defined per Equation 10

$$e^{ML}(\vec{p}) = \sum_{i=1}^m \|f_i^{ML}(\vec{p}, \vec{q}) - f_i^{mes}(\vec{q})\|_{L_2(Q)} \quad (10)$$

The solution to the optimization problem is then defined by Equation 11

$$\vec{p}^* = \arg \min_{\vec{p} \in S^n} \{e^{FM}(\vec{p})\} \quad (11)$$

where, \vec{p}^* is the best parameters vector and S^n is constrained searching domain.

The iterative search algorithm continues until either convergence tolerance, ε , or the maximum number of iterations exceed the specified limit. The search domain is specified for all n parameters, $S^n[\vec{s}^1 \ \vec{s}^2]$. First, the IMCMC algorithm samples randomly and stores k number of parameters sets, $\vec{p}^i \in S^n; i = 1, 2, \dots, k$. Then, the model error functions, $e^{FM}(\vec{p})$, are calculated and stored in error function vector, $\vec{\mathcal{E}}_{1 \times k} = \{e^{f^m}(\vec{p}^1), e^{f^m}(\vec{p}^2), \dots, e^{f^m}(\vec{p}^k)\}$. Then from the current error function vector, the lowest error value, $\min(\vec{\mathcal{E}}) = e^{f^m}(\vec{p}^*)$, and the corresponding set of parameters, \vec{p}^* , are identified. \vec{p}^* is chosen as the closest approximation of the solution to the global minima.

Using IMCMC in complex forward problems with a wide search range generally shows a slow convergence rate. Therefore, surrogate models are used to accelerate the entire process by finding local optimum regions. For this purpose, all the stored sets of parameters and corresponding error sets are used to train the surrogate-model.

We use fully connected deep network [49] to train the model by all parameter sets and their corresponding error functions. Equation 12 presents the mapping system of the trained surrogate-model.

$$\vec{f}^{sm} : (\vec{p}) \longrightarrow e^{fm}(\vec{p}, \vec{q}) \quad (12)$$

Once trained, we have a surrogate-model to obtain surrogate model error function, $e^{sm}(\vec{p})$, without the computational cost of forward model. To find the minimum of $e^{sm}(\vec{p})$, we use genetic algorithm (GA). Using GA, the local minima of the surrogate-model, \vec{p}^{sm} , is found per Equation 13

$$\vec{p}^{sm} = \arg \min_{\vec{p}} \{e^{sm}(\vec{p})\} \quad (13)$$

The local minima, \vec{p}^{sm} , is added to the sets of the parameter vectors, \vec{p} . Then the model error function, $e^{fm}(\vec{p}^{sm})$, is calculated using the forward model and added to the error function vector, $\vec{\mathcal{E}}$. If $e^{fm}(\vec{p}^{sm})$ is lower than the convergence tolerance, then the iterations are terminated. Otherwise, the best parameters set, \vec{p}^* , is updated and the following RS is executed.

New sets of parameter vectors are generated based on normal distribution in the neighborhood of poles, and their corresponding model error functions are evaluated. Using poles help in the search for the global minimum around all possible local minima. A total of j number of poles are chosen from the latest parameter vectors, \vec{p} to cover highest probable area. To choose the highest probable area, all \vec{p} are sorted based on the magnitude of their model error function (lowest to highest error). Then the poles are selected among the lowest error range. Since \vec{p}^* is the best answer it forms the first pole. The subsequent poles then are chosen corresponding to the top ranked population (e.g., 10% and 30%), $\vec{\mathfrak{P}} = \{\vec{p}^*, \vec{p}^2, \dots, \vec{p}^j\}$.

A total of g number of random parameter vectors is generated centered around each pole using a normal distribution. The generated parameter vectors are added to the entire parameter vectors. The forward model is then used to estimate the model error function for all newly added parameter vectors and \vec{p}^* is updated. Finally, the search domain is updated around \vec{p}^* per Equation 14

$$S^m[\vec{s}^1 \quad \vec{s}^2] = [a \times \vec{p}^* \quad b \times \vec{p}^*] \quad (14)$$

where a and b are coefficients adjusting the range. The surrogate model is trained again and iteration continues until the satisfying the convergence criteria is met or the maximum number of iterations is exceeded.

5. Result and discussion

In this section, we solve three examples to demonstrate the application of proposed method for estimating mechanical properties of solid materials. All three examples are propagation of stress waves into heterogeneous two dimensional media. In all examples, the mechanical properties are estimated by sending stress waves from two sides and capturing the strain response at two other

sides. Figure 3 schematically illustrates all three examples. In all examples, the experimental wave propagations were simulated by solving KT forward model and addition of 0.1% Gaussian noise. As measurements, the nodal strains vector is provided over certain boundaries. As the boundary conditions, for all examples shown, left and bottom edges, Γ , velocity controlled stress waves are injected and over right and top edges, Ψ , nodal strains are recorded as measurements. The velocity of the excitation wave over Γ is defined by Equation 15. It should be noted that the discretization of the simulated forward models and inverse models were different.

$$\begin{aligned} v(\eta, t) &= \sin(2\pi \times t); \quad \eta \in \Gamma & t \leq 1 \\ v(\eta, t) &= 0; \quad \eta \in \Gamma & t > 1 \end{aligned} \quad (15)$$

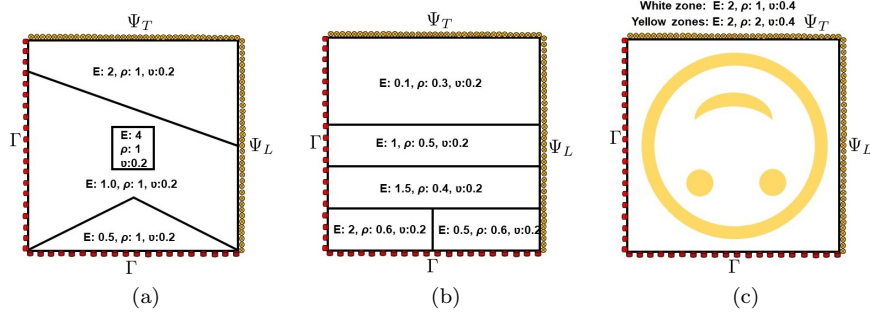


Figure 3: Schematic illustrations of all three simulated experiments.

5.1. Example 1

In the first example, Figure 3a, we assume the presence of prior knowledge about density and Poisson coefficient equal to 1 gr/cm^3 and 0.2 respectively. The objective is to estimate the nodal elastic moduli distributions in domain. In most tomography problems, the main objective is anomaly and damage detections. To achieve these objectives, most common approach is to calculate elastic or dynamic elastic moduli distributions over domains. Example 1, therefore, focuses on reconstruction of elastic moduli distributions over a domain using stress wave propagations. To do so, the deep learning network should be trained first to connect nodal elastic moduli to nodal strain measurements vector. Then, using deep learning surrogate IMCMC algorithm, distributions of elastic moduli will be reconstructed.

For this example, the deep learning input layer (L_0) is a vector of 10000 units using normalized nodal elastic modulus values. The output layer (L_H) is a vector of 202 units which uses normalized nodal strain values at Ψ_L and Ψ_T boundaries as is shown by Figure 3a. Total of 30 hidden layers were used in

deep learning network in this example where the number of units of these layers started from 10000 (L_1) and decreased gradually to 300 at the final hidden layer (L_{H-1}). L_2 regularization parameters were chosen using an initial batch of random parameter vectors as train and development sets to avoid overfitting. 25% dropout probability was chosen as the optimum regularization parameter. The momentum terms, learning rate and learning rate decay all were tuned by training the network based on initial random search batch. The estimated parameters at each iteration of inverse problem are divided into 10 mini-batches and each set of parameters generated statistically around poles are considered new mini-batches.

The deep learning based IMCMC algorithm starts with 100000 initial random parameter vectors batch as random batch. The search domain was initiated for elastic modulus, E between [1 20]. The training progress window were $a = 0.8$ and $b = 1.2$, which means that after surrogate model training, the search domain includes trial solutions within $\pm 20\%$ of the optimal solution. 10 statistical search poles were used, $j = 10$, around best parameter vector and best 5, 10, 15, 20, 25, 30, 35, 40, 45% parameter vectors. A total of $g = 2000$ random parameter vectors were generated at each pole. The convergence tolerance for this example was considered 10%. The deep learning search algorithm iterated while the lowest error function is higher than convergence tolerance. Figure 4a and 4b compare the true and the reconstructed elastic modulus distributions.

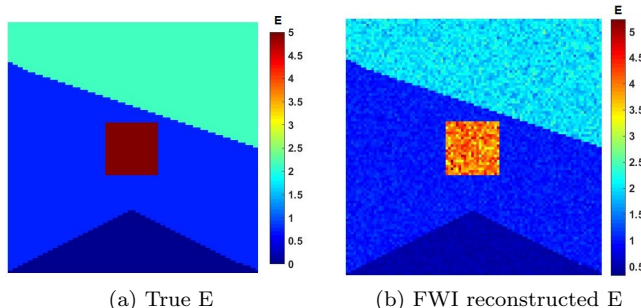


Figure 4: Nodal elastic moduli distribution of the domain shown by Figure 3a: (a) true elastic moduli, (b) reconstructed elastic moduli.

The results indicate that the reconstructed elastic moduli distribution is in good agreement with true elastic moduli. Comparing true and reconstructed results suggest average of 5% distributed error is measured between true and reconstructed elastic moduli distributions. Comparing these two images, reconstructed image provides proper distinction between different blocks of materials. Figure 5a presents measured nodal strain values at Ψ_T and Ψ_L boundaries over time, which were considered as optimization objectives between real and simulation cases. The whole time of 30 was simulated since it was sufficient to capture almost all propagation events inside the domain for FWI reconstructions. Figure 5b presents similar results for reconstructed elastic moduli distribution to

5a. The coverage norm between true measurements and estimated one at final iteration was 5.77% which means true and estimated measurements had average of $\pm 5.77\%$ difference at each time and space dimensions.

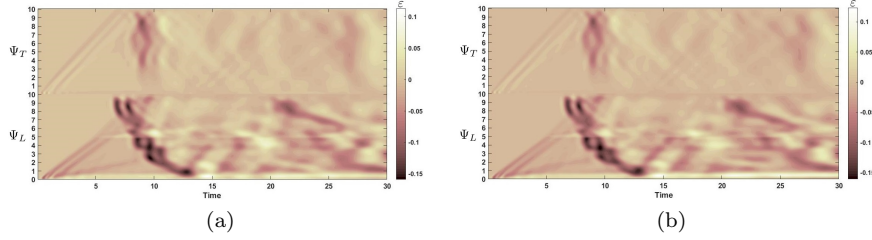


Figure 5: Nodal strain values at Ψ_T and Ψ_L boundaries with respect to time: (a) true strain measurements, and (b) reconstructed strain values.

Finally, Figure 6 presents comparison of wave velocity distributions between real and reconstructed domain at 1, 5, 10, 15 and 30 seconds. The top row of Figure 6 presents wave velocity distribution inside real domain at 1, 5, 10, 15 and 30 seconds respectively from left to right. The bottom row of Figure 6 presents wave velocity distribution inside reconstructed domain at 1, 5, 10, 15 and 30 seconds respectively from left to right. Similarly, Figure 6 suggests very good agreement between both situations.

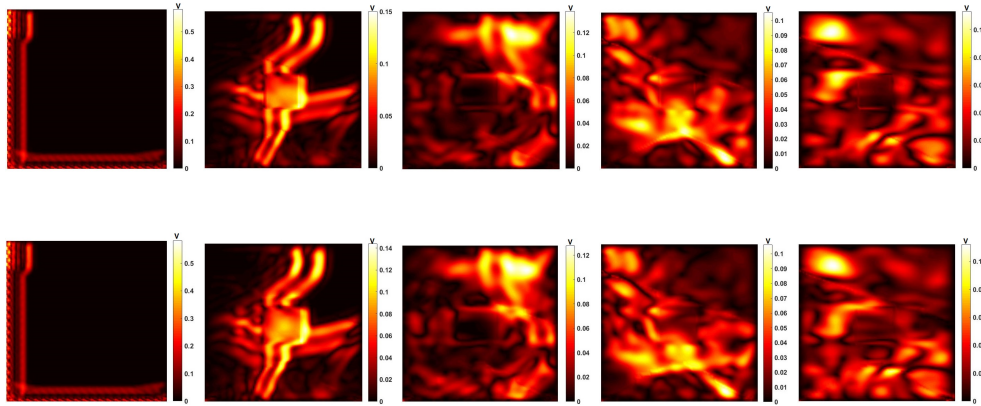


Figure 6: Wave velocity distribution inside domain: (top row) inside real domain at 1, 5, 10, 15 and 30 seconds respectively from left to right, (bottom row) inside FWI reconstructed domain at 1, 5, 10, 15 and 30 seconds respectively from left to right.

5.2. Example 2

In the second example, Figure 3b, we only assume prior information about Poisson coefficient equal to 0.2. Therefore, the objective is to estimate distri-

butions of elastic moduli and densities over the domain. Often, the objective of tomography problems exceeds to estimate real material properties. To achieve such objective, most common approach is to estimate wave velocity distributions over domains which contain effects of elastic modulus and density. Using common approaches of wave travel time, gradient based inverse methods, and generally qualitative tomographic methods, it is a very cumbersome objective to estimate elastic moduli and densities distribution at same time seperately. Also, due to probable high ill-posedness of inverse problem, it is not guaranteed to estimate the most optimum responses. To achieve this objective, here, the deep learning network was trained first to connect vector of nodal elastic moduli and densities to nodal strain measurements vector. Then, using the optimization of deep learning model, distributions of elastic moduli and densities are estimated at same time.

In this example, the deep learning input layer (L_0) was a vector of 20000 units uses normalized nodal elastic moduli and densities at same time. The output layer (L_H) is a vector of 202 units which uses normalized nodal strain values at Ψ_L and Ψ_T boundaries as is shown by Figure 3b. Total of 45 hidden layers were used in deep learning network in this example where the number of units of these layers started from 20000 (L_1) and decreased gradually to 202 at the final hidden layer (L_{H-1}). Similarly, L_2 regularization and dropout method were used. 35% dropout probability was chosen as the optimum regularization parameter. The dropout probability here was chosen higher than first example to introduce higher randomness and avoid vanishing issue in this example. Similar momentum terms, learning rate and learning rate decay were used in this example as example 1. After each inverse problem iteration, new parameters are divided into 10 mini-batches and each set of parameters generated statistically around poles are considered new mini-batches.

The deep learning based IMCMC starts with 300000 initial random parameter vectors batch as random batch. The search domain was initiated for elastic modulus, E between $[1 \ 20]$; and for density, ρ between $[0.001 \ 2]$ (used higher than zero to avoid singularity). The training window were $a = 0.8$ and $b = 1.2$ to search parameters within $\pm 20\%$ of the optimal solution in every iteration. 10 statistical search poles were used, $j = 10$, around best parameter vector and best 5, 10, 15, 20, 25, 30, 35, 40, 45% parameter vectors. A total of $g = 4000$ random parameter vectors were generated at each poles. The convergence tolerance for this example was considered 10%, however, the inverse problem had not converged to less than 10% before the iteration number exceeds iteration limit. Comparing true and reconstructed material properties, Figure 7 compares the true and the reconstructed elastic moduli and dnsities distributions.

According to Figure 7, the results indicate that the reconstructed elastic moduli and densities distributions are in agreement with true ones. Comparing true and reconstructed E results suggest average of 1.3% distributed error is measured between true and reconstructed elastic modulus distributions. Comparing true and reconstructed ρ results suggest average of 1% distributed error is measured between true and reconstructed density distributions. Comparing these two columns, proposed FWI deep learning method succeeded to recon-

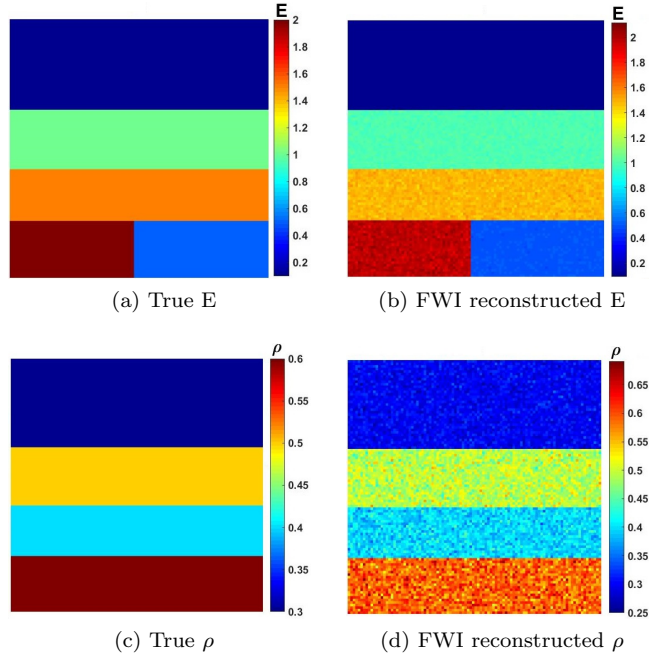


Figure 7: (a) True elastic moduli distribution, (b) FWI reconstructed elastic moduli distribution, (c) True densities distribution, (d) FWI reconstructed densities distribution.

struct both E and ρ distributions simultaneously.

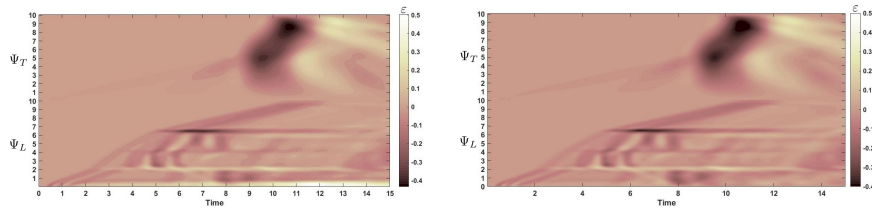


Figure 8: Nodal strain values at Ψ_T and Ψ_L boundaries with respect to time: (a) true strain measurements, and (b) FWI reconstructed measurements.

Figure 8 presents measured nodal strain values over Ψ_T and Ψ_L at whole 15 time range which were considered as optimization objectives between real and simulation cases. The coverage norm between true measurements and estimated one at final iteration was 14.99% which means variation of estimated measurement is $\pm 14.99\%$ to true measurements. In this example, the coverage condition of 10% has not been met. Therefore, after iterations exceeded iteration limit, the inverse problem was terminated. Reconstruction of both densities and elastic moduli at the same time introduces higher ununiqueness and non-

convexity to the inverse problem. That is why the inverse problem was not able to converge to the 10% $L - 2$ norm convergence. Comparing two results of Figure 8, measurements are still comparable.

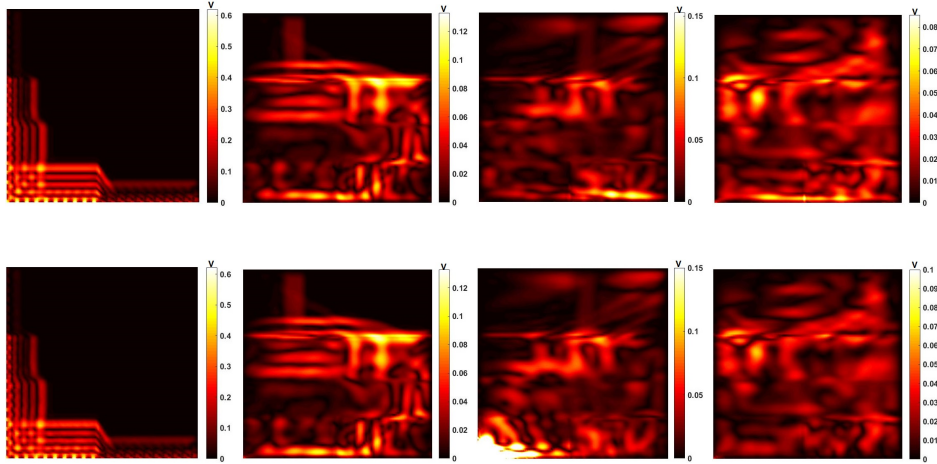


Figure 9: Wave velocity distribution inside domain: (top row) inside real domain at 1, 5, 10 and 15 seconds respectively from left to right, (bottom row) inside FWI reconstructed domain at 1, 5, 10 and 15 seconds respectively from left to right.

Finally, Figure 9 presents comparison of wave velocity distributions between real and reconstructed domain at 1, 5, 10 and 15 seconds. The top row of Figure 9 presents wave velocity distribution inside real domain at 1, 5, 10 and 15 seconds respectively from left to right. The bottom row of Figure 9 presents wave velocity distribution inside reconstructed domain at 1, 5, 10 and 15 seconds respectively from left to right. Reconstructing both densities and elastic moduli at the same time using transient wave propagation can be cumbersome for many reasons. First, simulation of wave propagation through realistic detailed volumetric representations of heterogeneous materials is cumbersome because of the huge computational requirements for higher order simulation methods and high chance of instability of lower order methods. Numerical methods to accurately simulate the wave equation are being constantly developed and applied with increasing levels of sophistication. KT, has been shown to be an efficient method for simulation of nonlinear conservation differential equations with high resolution and can handle high scattering and shock waves. Second, variation of density and elastic modulus together can raise a huge amount of non-convexity. Here, comparing results, shows that using proposed deep learning based inverse model and KT forward model have been able to handle these complexities.

5.3. Example 3

In the third example, Figure 3c, we consider Poisson coefficient equal to 0.2 and known nodal elastic moduli, therefore, the objective is to estimate densities distribution of the domain. This can be helpful for cases that different materials with different densities have similar elastic moduli. For this example, similar model of deep learning to example 1 was used. However, wave propagation simulation is more sensitive to variation of densities than variation of elastic moduli. Also, variation of densities cause higher ill-posedness of inverse problem. Therefore, here, the deeper learning network was trained to connect vector of nodal densities to the nodal strain measurements.

Similar to example 1, the deep learning input layer (L_0) was a vector of 10000 units uses normalized nodal elastic moduli and densities at same time. The output layer (L_H) is a vector of 202 units which uses normalized nodal strain values at Ψ_L and Ψ_T boundaries as is shown by Figure 3b. Total of 30 hidden layers were used in deep learning network in this example where the number of units of these layers started from 10000 ((L_1)) and decreased gradually to 202 at the final hidden layer (L_{H-1}). Similarly, L_2 regularization and dropout method were used. 30% dropout probability was chosen as the optimum regularization parameter. The dropout probability here was chosen higher than first example to introduce higher randomness in this example. Similar momentum terms, learning rate and learning rate decay were used in this example as example 1. The RS based parameters are divided into 10 mini-batches and each set of parameters generated statistically around poles are considered new mini-batches.

The deep learning based ICMC algorithm starts with 100000 initial random parameter vectors batch as random batch. The search domain was initiated for density, ρ between [0.001 5] (used higher than zero to avoid singularity). The training progress window were $a = 0.8$ and $b = 1.2$ to search RS parameters within $\pm 20\%$ of the optimal solution in every iteration. 10 statistical search poles were used, $j = 10$, around best parameter vector and best 5, 10, 15, 20, 25, 30, 35, 40, 45% parameter vectors. A total of $g = 4000$ random parameter vectors were generated at each poles. Comparing true and reconstructed material properties, Figure 10 compares the true and the reconstructed densities distributions.

According to Figure 10, the results indicate that the reconstructed densities distributions are in agreement with true ones. Comparing true and reconstructed ρ results suggest average of 3.2% distributed error is measured between true and reconstructed elastic modulus distributions. Comparing these results, proposed method succeeded to reconstruct ρ distributions in good agreement to the real case.

Figure 11 presents measured nodal strain values over Ψ_T and Ψ_L at whole 30 time range which were considered as optimization objectives between real and simulation cases. The coverage norm between true measurements and estimated one at final iteration was 8.7% which means variation of estimated measurement is $\pm 8.7\%$ to true measurements.

Finally, Figure 12 presents comparison of wave velocity distributions between real and reconstructed domain at 1, 5, 10, 15 and 30 seconds. The top

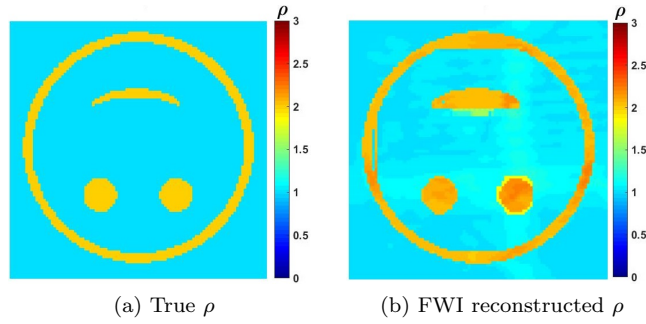


Figure 10: (a) True densities distribution, (b) FWI reconstructed densities distribution.

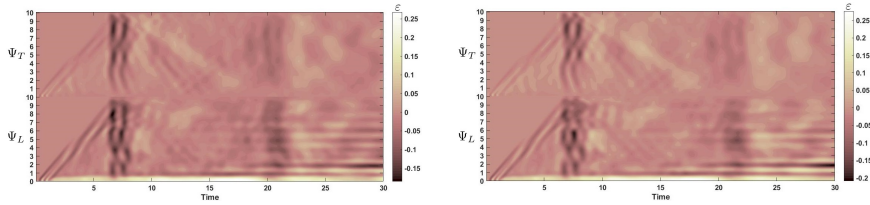


Figure 11: Nodal strain values at Ψ_T and Ψ_L boundaries with respect to time: (a) true strain measurements, and (b) FWI reconstructed measurements.

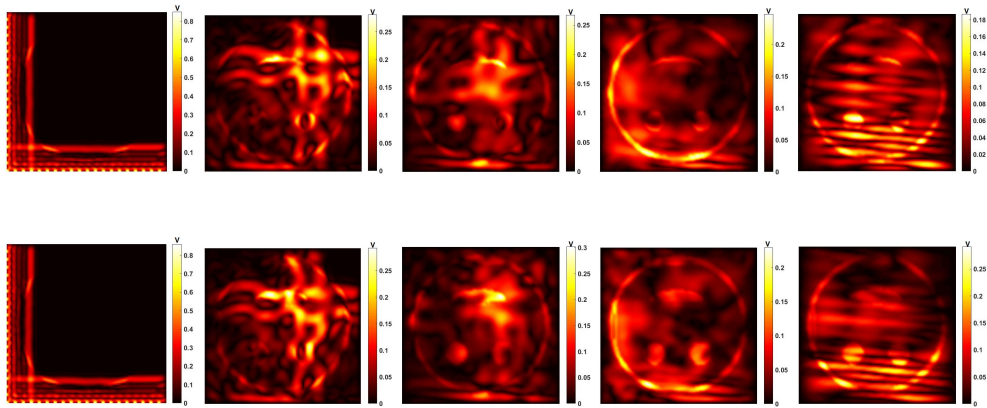


Figure 12: Wave velocity distribution inside domain: (top row) inside real domain at 1, 5, 10, 15 and 30 seconds respectively from left to right, (bottom row) inside FWI reconstructed domain at 1, 5, 10, 15 and 30 seconds respectively from left to right.

row of Figure 12 presents wave velocity distribution inside real domain at 1, 5, 10, 15 and 30 seconds respectively from left to right. The bottom row of

Figure 12 presents wave velocity distribution inside reconstructed domain at 1, 5, 10, 15 and 30 seconds respectively from left to right. Reconstructing both densities and elastic moduli at the same time using transient wave propagation can be cumbersome for main two reasons. First, simulation of wave propagation through realistic detailed volumetric representations of heterogeneous materials is cumbersome because of the huge computational requirements for higher order simulation methods and high chance of instability of lower order methods. Numerical methods to accurately simulate the wave equation are being constantly developed and applied with increasing levels of sophistication. Kurganov-Tadmor, has been shown to be an efficient method for simulation of nonlinear conservation differential equations with high resolution and can handle high scattering and shock waves. Second, variation of density and elastic modulus together can raise huge amount of non-convexity. Here, comparing results, shows that using proposed deep learning based inverse model and KT forward model have been able to handle these complexities.

6. Conclusions

We proposed a deep learning surrogate IMCMC algorithm for quantitatively estimating the mechanical properties in heterogeneous media. In this inverse problem, we utilized high resolution central scheme, Kurganov-Tadmor (KT), as a forward model for stress wave propagation. This forward model well handles material heterogeneity and gradients. While this inverse problem is ill-posed and non-convex, this algorithm is successfully used to estimate the mechanical properties. This approach is used instead of end to end deep learning model for connecting nodal strain measurements to nodal elastic moduli due to high ill-posedness and lower accuracy of reconstructions. Comparing results of reconstructions to real values suggest the deep learning surrogate IMCMC method is able to quantify material characteristics properly.

References

- [1] S. Bagavathiappan, B. Lahiri, T. Saravanan, J. Philip, T. Jayakumar, Infrared thermography for condition monitoring a review, *Infrared Physics & Technology* 60 (2013) 35–55.
- [2] B. Lahiri, S. Bagavathiappan, T. Jayakumar, J. Philip, Medical applications of infrared thermography: A review, *Infrared Physics & Technology* 55 (4) (2012) 221–235.
- [3] R. Rashednia, O. Khalaf Alla, G. Gonzalez-Berrios, A. Seppänen, M. Pour-Ghaz, Electrical resistance tomographybased sensing skin with internal electrodes for crack detection in large structures, *Materials Evaluation* 76 (10) (2018) 1405–1413.

- [4] R. Rashednia, D. Smyl, M. Hallaji, A. Seppänen, M. Pour-Ghaz, Structural health monitoring using electrical resistance tomography based sensing skin: Detecting damage, corrosive elements, and temperature change, in: *The 9th International Conference on Inverse Problems in Engineering (ICIPE)*, 2017.
- [5] D. Smyl, R. Rashednia, A. Seppänen, M. Pour-Ghaz, Can electrical resistance tomography be used for imaging unsaturated moisture flow in cement-based materials with discrete cracks?, *Cement and Concrete Research* 91 (2017) 61–72.
- [6] R. Rashednia, M. Hallaji, D. Smyl, A. Seppänen, M. Pour-Ghaz, Detection and localization of changes in two-dimensional temperature distributions by electrical resistance tomography, *Smart Materials and Structures* 26 (11) (2017) 115021.
- [7] B. Brown, Electrical impedance tomography (eit): a review, *Journal of Medical Engineering & Technology* 27 (3) (2009) 97–108.
- [8] R. Davalos, D. Otten, L. Mir, B. Rubinsky, Electrical impedance tomography for imaging tissue electroporation, *IEEE Transactions on Biomedical Engineering* 51 (5) (2004) 761–767.
- [9] L. Borcea, Electrical impedance tomography, *Inverse Problems* 18 (6) (2002) R99R136.
- [10] A. Voss, N. Hänninen, M. Pour-Ghaz, M. Vauhkonen, A. Seppänen, Imaging of two-dimensional unsaturated moisture flows in uncracked and cracked cement-based materials using electrical capacitance tomography, *Materials and Structures* 51 (3) (2018) 68.
- [11] A. Voss, M. Pour-Ghaz, M. Vauhkonen, A. Seppänen, Difference reconstruction methods for electrical capacitance tomography imaging of two-dimensional moisture flow in concrete, in: *The 9th international conference on inverse problems in engineering (ICIPE)*, Waterloo, Canada, 2017.
- [12] O. Büyükköztürk, Imaging of concrete structures, *Non-Destructive Testing & Evaluation International* 31 (4) (1998) 233–243.
- [13] L. Topczewski, F. Fernandes, P. Cruz, P. Lourenco, Practical implications of gpr investigation using 3d data reconstruction and transmission tomography, *Journal of Building Appraisal* 3 (1) (2007) 59–76.
- [14] G. Balazs, E. Lubloy, T. Földes, Evaluation of concrete elements with x-ray computed tomography, *Journal of Materials in Civil Engineering* 30 (9) (2018) 06018010.
- [15] F. Mees, R. Swennen, M. Van Geet, P. Jacobs, Applications of x-ray computed tomography in the geosciences, *Geological Society of London* 215 (2003) 1–6.

- [16] R. Ketcham, W. Carlson, Acquisition, optimization and interpretation of x-ray computed tomographic imagery: applications to the geosciences, *Computers & Geosciences* 27 (4) (2001) 381–400.
- [17] H. Choi, S. Popovics, Nde application of ultrasonic tomography to a full-scale concrete structure, *IEEE Transactions on Ultrasonics, Ferroelectrics, and Frequency Control* 62 (6) (2015) 1076–1085.
- [18] S. Lin, S. Shams, H. Choi, H. Azari, Ultrasonic imaging of multi-layer concrete structures, *Nondestructive Testing & Evaluation International* 98 (2018) 101–109.
- [19] M. Krause, F. Mielentz, B. Milman, W. Muller, V. Schmitz, H. Wiggenhauser, Ultrasonic imaging of concrete members using an array system, *Nondestructive Testing and Evaluation International* 34 (2001) 403–408.
- [20] M. Schickert, Progress in ultrasonic imaging of concrete, *Materials and Structures* 38 (2005) 807–815.
- [21] A. Haza, A. Samokrutov, P. Samokrutov, Assessment of concrete structures using the mira and eyecon ultrasonic shear wave devices and the soft-c image reconstruction technique, *Construction and Building Materials* 38 (2013) 1276–1291.
- [22] S. Beniwal, D. Ghosh, A. Ganguli, Ultrasonic imaging of concrete using scattered elastic wave modes, *Nondestructive Testing and Evaluation International* 82 (2016) 26–35.
- [23] P. Liu, P. Yeh, Vertical spectral tomography of concrete structures based on impact echo depth spectra, *Nondestructive Testing and Evaluation International* 43 (2010) 45–53.
- [24] P. Liu, P. Yeh, Spectral tomography of concrete structures based on impact echo depth spectra, *Nondestructive Testing and Evaluation International* 44 (2011) 692–702.
- [25] J. Zhu, J. Popovics, Imaging concrete structures using air-coupled impact-echo, *JOURNAL OF ENGINEERING MECHANICS* 133 (2007) 628–640.
- [26] T. Yu, J. Chaix, L. Audibert, D. Komatitsch, V. Garnier, J. Henault, Simulations of ultrasonic wave propagation in concrete based on a two-dimensional numerical model validated analytically and experimentally, *Ultrasonics* 92 (2019) 21–34.
- [27] S. Beniwal, A. Ganguli, Defect detection around rebars in concrete using focused ultrasound and reverse time migration, *Ultrasonics* 62 (2015) 112–125.

- [28] H. Liu, H. Xia, M. Zhuang, Z. Long, C. Liu, J. Cui, B. Xu, Q. Hu, Q. Liu, Reverse time migration of acoustic waves for imaging based defects detection for concrete and cfst structures, *Mechanical Systems and Signal Processing* 117 (2019) 210–220.
- [29] K. Kawashima, M. Murase, R. Yamada, M. Matsushima, M. Uematsu, F. Fujita, Nonlinear ultrasonic imaging of imperfectly bonded interfaces, *Ultrasonics* 44 (2006) 1329–1333.
- [30] R. Rashetnia, F. Ghasemzadeh, M. Hallaji, M. Pour-Ghaz, Quantifying prestressing force loss due to corrosion from dynamic structural response, *Journal of Sound and Vibration* 433 (2018) 129–137.
- [31] S. Law, Z. Lu, Time domain responses of a prestressed beam and prestress identification, *Journal of Sound and Vibration* 288 (2005) 1011–1025.
- [32] Z. Lu, S. Law, Identification of prestress force from measured structural responses, *Mechanical Systems and Signal Processing* 20 (2006) 2186–2199.
- [33] R. Rashetnia, F. Ghasemzadeh, M. Pour-Ghaz, The consequences of material nonlinearity on the axisymmetric flexural vibration measurements for estimating the dynamic elastic modulus of damaged cement based materials, *Journal of Advanced Concrete Technology* 14 (6) (2016) 287–298.
- [34] A. Guitton, Blocky regularization schemes for full waveform inversion, *Geophysical Prospecting* 60 (5) (2012) 870–884.
- [35] W. Hu, A. Abubakar, T. Habashy, Simultaneous multifrequency inversion of full-waveform seismic data, *Geophysics* 74 (2009) 1–14.
- [36] Y. Lin, L. Huang, Acoustic- and elastic-waveform inversion using a modified total-variation regularization scheme, *Geophysical Journal International* 200 (1) (2015) 489–502.
- [37] Y. Lin, L. Huang, Quantifying subsurface geophysical properties changes using double-difference seismic waveform inversion with a modified total-variation regularization scheme, *Geophysical Journal International* 203 (3) (2015) 2125–2149.
- [38] D. Vigh, E. Starr, Comparisons for waveform inversion, time domain or frequency domain?, 78th Annual International Meeting, SEG (2008) 1890–1894.
- [39] W. Lewis, D. Vigh, Deep learning prior models from seismic images for full-waveform inversion, in: *SEG Technical Program Expanded Abstracts*, 2017, pp. 1512–1517.
- [40] A. Richardson, Seismic full-waveform inversion using deep learning tools and techniques, arXiv (2018) 1801.07232.

- [41] J. Virieux, S. Operto, An overview of fullwaveform inversion in exploration geophysics, *Geophysics* 74 (2009) WCC1WCC26.
- [42] A. Kurganov, E. Tadmor, New high-resolution central schemes for nonlinear conservation laws and convection-diffusion equations, *Journal of Computational Physics* 160 (1) (2000) 241–282.
- [43] V. Rusanov, The calculation of the interaction of non-stationary shock waves with barriers, *Z. Vycisl. Mat. i Mat. Fiz.* 1 (1961) 267–279.
- [44] B. Van Leer, Towards the ultimate conservative difference scheme, v. a second order sequel to godunov’s method, *Journal of Computational Physics* 32 (1) (1979) 101–136.
- [45] P. Lax, Weak solutions of nonlinear hyperbolic equations and their numerical computation, *Communications on Pure and Applied Mathematics* 7 (1) (1954) 159–193.
- [46] H. Nessyahu, E. Tadmor, Non-oscillatory central differencing for hyperbolic conservation laws, *Journal of Computational Physics* 87 (2) (1990) 408–463.
- [47] P. Tahmasebi, F. Javadpour, M. Sahimi, Stochastic shale permeability matching: Three-dimensional characterization and modeling, *International Journal of Coal Geology* 165 (2016) 231–242.
- [48] P. Del Moral, Mean field simulation for Monte Carlo integration, Chapman & Hall/CRC Monographs on Statistics and Applied Probability, 2013.
- [49] W. Chow, S. Cho, Neural networks and computing: Learning algorithms and applications, Imperial college press, 2007.